Pseudomorphic Crystal Growth of the Model Steroid Methyl Analogue of Norethindrone

S. X. M. Boerrigter, C. J. M. van den Hoogenhof, H. Meekes,* P. Verwer, and P. Bennema

NSRIM, Department of Solid State Chemistry, University of Nijmegen, Toernooiveld 1, 6525 ED Nijmegen, The Netherlands

Received: December 5, 2001; In Final Form: September 4, 2002

Various morphologies of two polymorphs of a steroid are observed and correlated to calculated morphologies using the connected net theory. In a previous publication on our model compound, we reported polymorphic epitaxial growth as a result of variations in the supersaturation. Two additional and also unusual types of growth behavior are described in this work: the observation of crystals that have a morphology that does not correspond to its observed polymorph, also called pseudomorphism, and the observation of a particular crystal face on which distinctive faceted pits occurred. The particular kinetic growth behavior of this model compound is explained by the fact that the two polymorphs are partly isostructural and by impurity induced growth hampering.

1. Introduction

It is well-known that many organic crystals exhibit polymorphism. This may cause problems for crystallization processes because different polymorphs can sometimes be formed at very similar growth conditions.[1] Though interesting, the occurrence of polymorphism can have major drawbacks. If one specific polymorph is desired, it is important to know and understand the conditions for the formation of such a specific polymorph. Particularly, the different growth kinetics for polymorphs play an important role but are usually not well understood. Polymorphism can also give rise to unwanted morphologies because different polymorphs very often have completely different morphologies. We therefore present in this paper the study of the relation between polymorphism, morphology, and crystal growth mechanisms of a test compound.

Many steroids show polymorphism as can be seen from a search in the Cambridge Structural Database (CSD).[2,3] As a test compound, the polymorphic steroid 7-α-methyl Δ5,10-norethindrone (7αMNa), which serves as a pharmaceutical compound for hormone replacement therapy, was chosen. Two polymorphs have been elucidated, namely, a monoclinic phase with space group $P2_1$ and a triclinic phase ($P1$),[4,5] which both can be found in the CSD.

As a rule of thumb, the $P1$ phase can be obtained from apolar solvents such as hexane resulting in a needlelike habit, whereas the $P2_1$ phase can be obtained from polar media like acetone and acetonitril yielding a bulky habit. Previously, we described crystal growth experiments performed from acetone.[6] In that work, the unusual phenomenon of polymorphic epitaxial growth was described, as well as the relationship between the two polymorphs in terms of their thermodynamics and kinetics. In short, the polymorphic epitaxial growth can be described as the 2D nucleation of the metastable phase onto the stable phase. In our case, the $P1$ phase nucleated on the (010) face of the $P2_1$ crystal above a certain threshold supersaturation. Moreover, it was shown that acetone acts as a mediating solvent strongly inducing the transformation of $P1$ to $P2_1$ in time and, thus, plays an important role in the kinetics. Consequently, the solvent used in that work also plays an ambiguous role on the morphological results. To rule out this factor completely and to gain more understanding of crystal growth and morphology, crystals were grown from the vapor phase and compared with calculated morphologies. The latter should correspond best to the morphology of crystals in a vacuum because they do not include the solvent in the model.

TABLE 1: Crystal Data of Both 7αMNa Polymorphs

	polymorph (CSD refcode)		
	$P2_1$ (CIYRIL00)	$P1$ (CIYRIL01)	$P1_{trans}$; $\chi = 1$ (4)
a (Å)	6.542	6.542	6.542
b (Å)	41.213	6.6773	10.287 (41.148)
c (Å)	6.678	10.287	6.677
α (deg)	90	87.05	92.95
β (deg)	101.64	80.09	100.83
γ (deg)	90	79.17	80.09
D_x (g cm^{-3})	1.18	1.194	1.194
Z	4	1	1 (4)
Z'	2	1	1

2. 7αMNa Crystal Structures

The crystallographic data of the two known polymorphic forms are summarized in Table 1. At first sight, the two structures are completely different. However, using the transformation

$$(\mathbf{a},\mathbf{b},\mathbf{c})_{P1\text{trans}} = (\mathbf{a},\mathbf{b},\mathbf{c})_{P1}\begin{pmatrix}1 & 0 & 0\\ 0 & 0 & \chi\\ 0 & \bar{1} & 0\end{pmatrix} = (\mathbf{a},\bar{\mathbf{c}},\chi\mathbf{b})_{P1}$$

on the crystallographic axes produces an alternative setting of the triclinic structure, showing the similarity between the two structures. A value of $\chi = 1$ gives the normal size unit cell; $\chi = 4$ produces a unit cell with similar dimensions as the $P2_1$ unit cell. In this setting, both structures consist of densely packed layers of molecules in the *ac* plane, which are connected by hydrogen bonds. Figure 1 shows both structures in the same orientation after applying the transformation on $P1$. Obviously, in $P1$, every layer has the same orientation. The orientation of

* To whom correspondence should be addressed. E-mail: hugom@sci.kun.nl.

10.1021/jp014416q CCC: $22.00
Published on Web 12/02/2002

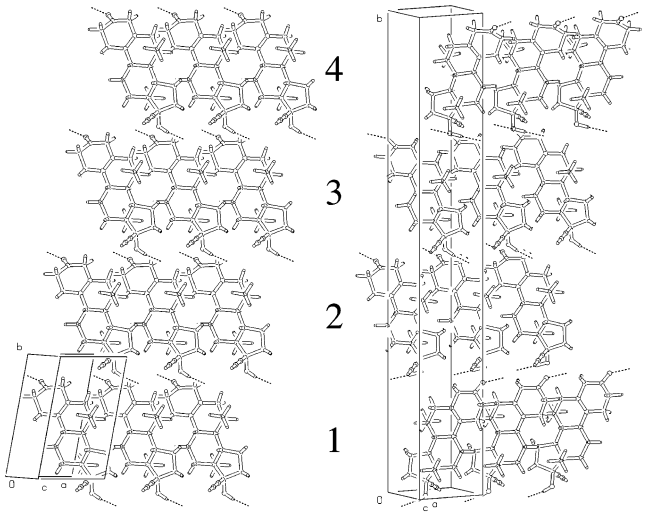

Figure 1. The two structures of 7αMNa (left, *P*1; right, $P2_1$) showing four layers of the hydrogen-bridged steroids. Layers 2 and 3 of both structures have an identical orientation and an identical hydrogen bridging between them with identical conformations of the respective H-bond donors and acceptors. The connection between layers 3 and 4 (thus also 1 and 2) introduces conformational changes needed to maintain the hydrogen bonds in the $P2_1$ structure. Layers 1 and 3, as well as 2 and 4, of the $P2_1$ structure are related by the 2-fold screw axis.

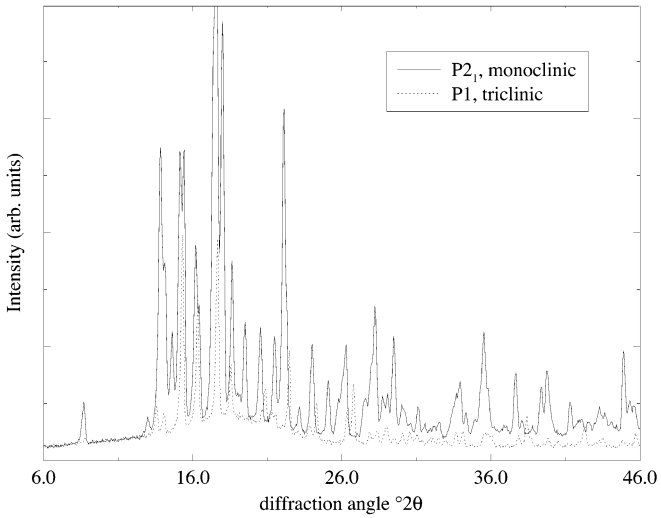

Figure 2. Calculated X-ray powder diffractograms of the pure *P*1 and $P2_1$ crystal phases of 7αMNa at equal attenuation. The diffractograms show that most peaks of the *P*1 phase are covered by those of the $P2_1$ phase.

the molecules in layers 2 and 3 in $P2_1$ is identical, whereas in layers 1 and 4, the $P2_1$ layers are rotated 180° by the screw axis perpendicular to the layers. To maintain the hydrogen bonding in $P2_1$, an interesting conformational difference between the two structures is needed causing the larger asymmetric unit in $P2_1$. Inspecting the hydrogen bonds between layers 2 and 3 shows that the structures overlap perfectly. However, ring A (six-membered uppermost ring) of the molecules in layer 3 is flipped from the 2α 3β half-chair into the 2β 3α half-chair conformation.[4] This dramatically changes the position of the H-bond-accepting carboxyls causing it to point forward (F orientation) with respect to the plane of view instead of backward (B orientation). Also, the overall orientation of the H-bond-donating hydroxyls is rotated completely (best seen by comparing the lower half of layer 2). Regarding the orientation of the molecules in the layers, the *P*1 structure has a ···BBBB··· stacking and the $P2_1$ structure stacks according to the repetitive pattern ···FBBFFBBF···. A slight shift in the position of the relative layers 1−2 and 3−4 causes the mismatch of the *b* axis, which gives rise to a notable difference of 10° in the angle γ, whereas the other unit cell parameters are nearly identical. For convenience, all further reference to the *P*1 structure and the corresponding morphological planes will be in the transformed setting with $\chi = 1$.

3 Experimental Section

3.1. Crystal Growth and Characterization. For the vapor-phase growth, the compound was introduced into a glass tube together with a copper wire, which served as a substrate. The tube was evacuated to about 9×10^{-6} mbar. The tube was then sealed by melting the end and placed in a furnace at approximately 383 K. The crystals were allowed to grow for 90 h. A more detailed description of this vapor-phase method can be found in the work of Bögels et al.[7] and references therein. It is important to note that in this setup part of the copper substrate resides outside of the furnace. As a result of the thermal conductivity, this creates a thermal gradient along the substrate. In turn, this creates a gradient in supersaturation along the substrate. The tube is introduced into the furnace such that the initial compound was approximately in the hottest area of the furnace, allowing for appreciable sublimation. Deposition takes place along the temperature gradient, resulting in a relatively small area in which faceted crystal growth took place. As a result of this setup, the absolute temperatures of the vapor and substrate are unknown, and therefore, only qualitative data on supersaturation is available.

The two main features of interest are the polymorphic form and the morphology of the crystals. Because of the design of the setup, vapor grown crystals could only be characterized ex situ. The methods used were X-ray powder diffraction, optical microscopy, scanning electron microscopy (SEM), and Raman spectroscopy. As a result of the similarity of the two structures, most X-ray peaks of the *P*1 structure overlap the $P2_1$ peaks but not vice versa (see also the calculated diffractograms in Figure 2). Hence, the determination of the purity of the *P*1 phase is straightforward, whereas the presence of traces of *P*1 cannot adequately be found within a sample of the $P2_1$ phase. On the other hand, Raman spectroscopy is a powerful technique to identify the two polymorphs by the peak splitting as a result of the multiple conformers in $P2_1$.[6]

The morphology of some crystals that were sufficiently large could be measured using an optical goniometer. With this instrument, the angles between crystal faces can be determined with an accuracy better than 0.5°.

3.2. Computational Methods. The following procedure was followed for the calculation of Hartman−Perdok (HP) morphologies. The Dreiding 2.21[8] force field was used for all molecular mechanics calculations in this study. Atomic charges were derived by fitting the electrostatic potential using the RESP method[9] on the geometry obtained by a Gaussian 94[10] optimization at the HF 6-31G* level. With these charges, a molecular-mechanics energy minimization was carried out to relax both crystal structures thereby avoiding close contacts.

These structures were used to calculate the interaction energies between the growth units. For convenience and to follow the terminology of Hartman and Perdok, the molecular interactions are called bonds. The growth units correspond to the individual molecules, giving the *P*1 structure 1 and the $P2_1$ structure 4 growth units, which are numbered 1−4, increasing along the positive *b* axis of the unit cell (see Figure 1). The

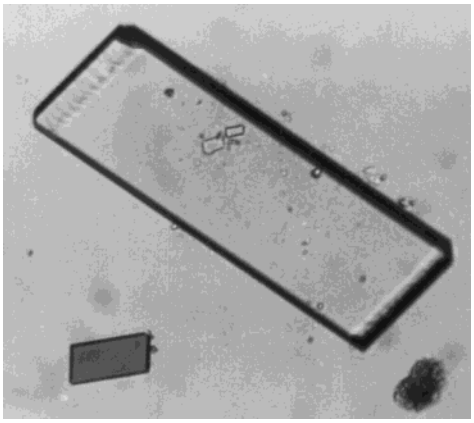

Figure 3. Example morphology of monoclinic 7αMNa grown from an acetone solution. Thin platelets are formed with the 2-fold axis perpendicular to the view plane.

crystal graph was defined by selecting all bonds stronger than −0.6 kcal/mol (a threshold of kT at 300 K[11]). The crystal graph was used as the input for the program FACELIFT-2.50.[12] Briefly, FACELIFT searches for periodic bond chains (PBCs),[13−15] combines these into connected nets,[16] and calculates their attachment energies. The so-called HP/E_{att} morphologies were created by making the Wulff construction using the common assumption of a linear dependency of the growth rate on the attachment energy ($R_{hkl} \propto E_{att}^{hkl}$). Note that this method can also be applied in a fully automated setup within the Cerius[2] environment using the Hartman−Perdok (HP) module.[17] Also note that the number of connected nets found strongly depends on the number of bonds in the crystal graph. Because the cutoff limit of −0.6 kcal/mol is arguable, alternative crystal graphs were produced using a much lower limit, which increased the number of bonds. This did produce a large amount of additional connected nets, but these were all very weak and did not contribute to the resulting morphology. This indicates that convergence of the resulting morphology was reached as a function of the energetic cutoff.

4 Results

4.1. Experimental Results. The crystals grown from acetone at moderate supersaturation appear as platelets with a 2-fold axis perpendicular to the basal face. The side faces change slightly in relative morphological importance as a function of the supersaturation, causing variation of the aspect ratio (see Figure 3). Only at higher supersaturations the morphology changes dramatically because of roughening of specific crystal faces and polymorphic epitaxial growth. This and a full description of the theoretical basis on these kinetically governed growth phenomena are described in detail in an earlier publication.[6]

Surprisingly, it was found that the morphology of the crystals grown from the vapor is completely different from crystals grown from acetone and, in fact, any other solution observed so far. On the copper substrate, three regions were found. The region with the lowest supersaturation shows very small needlelike crystals (∼10 μm). In the region with the highest supersaturation, a layer of very small crystallites or even amorphous material was deposited on the substrate. Both of the outer regions clearly did not provide the conditions to grow large, faceted crystals. However, in the middle of the substrate, crystals were grown of considerable size (up to 500 μm). An example of the typical blocklike crystals grown from the vapor phase is presented in Figure 4. An indication of internal stress

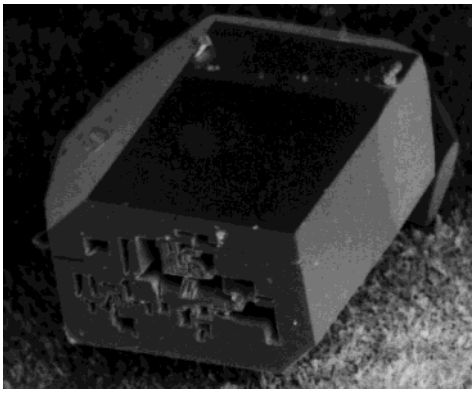

Figure 4. SEM image of a typical crystal grown from the vapor phase at moderate supersaturation. The size of this crystal is approximately 70 × 50 × 50 μm³. Faceted holes form an irregular pattern on the front face.

TABLE 2: Morphology of 7αMNa Grown from Vapor Fitted against the $P1$ and $P2_1$ Settings

facet	$P1$ face	misfit (deg)	$P2_1$ face	misfit (deg)
1	$(10\bar{1})$	2.961	$(10\bar{1})$	0.6211
2	$(\bar{1}00)$	4.526	(021)	0.7405
3	$(\bar{1}00)$	5.880	(011)	0.2682
4	(010)	13.34	$(01\bar{0})$	0.3693
5	$(11\bar{0})$	4.968	$(02\bar{1})$	0.3939
6	$(00\bar{1})$	5.591	$(1\bar{2}0)$	0.2994
7	$(0\bar{1}1)$	3.224	$(\bar{1}20)$	0.0395
8	$(\bar{1}01)$	2.849	$(\bar{1}01)$	0.7457
9	(011)	2.854	$(\bar{1}20)$	0.6547
10	$(0\bar{1}1)$	4.287	$(\bar{1}20)$	2.274
11	$(1\bar{1}0)$	6.214	$(0\bar{2}1)$	1.860
12	$(1\bar{1}1)$	6.760	$(1\bar{4}1)$	5.936

in these crystals was observed as, occasionally, the crystals violently cracked up during handling. Also in the SEM, many crystals broke up or sprang of the substrate. A few of the larger crystals could be measured using the optical goniometer, which showed that they fitted the $P2_1$ setting quite well except for the facets 11 and 12, as well as number 10 (see Table 2). Facets 11 and 12 were very small and hardly visible which accounts for their misorientation. In contrast, face 10 is a large and well-defined crystal face (rear part of the right-hand side of the crystal in Figure 4), which did not fit any crystallographic orientation ($\bar{h}kl$) within reason. Therefore, it is fitted to the closest face $(\bar{1}20)$ with a misfit angle of 2.3°. Fitting the face orientations to the rational indices of the $P1$ structure showed clearly that this is not the correct crystal structure because none of the faces even fitted within 2° after refinement. It should be noted that the listed $P1$ fit is constrained to indices $|h|, |k|, |l| \leq 1$, because increasing the range of allowed indices only produced unrealistic fit orientations. Raman measurements confirmed that the crystals indeed consisted of the $P2_1$ structure.

Almost all crystals, except for some smaller ones, showed an unusual surface morphology of the (010) face, namely, the appearance of faceted pits, which formed an irregular pattern. The pits in these patterns are faceted according to the orientation of the facets on the outside of the crystal. Thorough inspection showed that these pits were never formed on the opposite side of the crystal, the $(0\bar{1}0)$ face, or on any other crystal face. Note that the (010) and $(0\bar{1}0)$ can be distinguished by the fact that they are mirror images of each other. These pit patterns were repeatedly found in different vapor growth experiments and are a distinctive feature of these crystals. Due to the construction of the furnace, the formation of the pits could not be observed in situ. Therefore, it is not immediately obvious at which stage of the experiments the pits are formed and whether it is a growth

TABLE 3: Reduced Crystal Graph of the *P*1 Structure, Which Represents All Strong Interactions between the Growth Units (GU)[a]

GU1−GU2	translation	E_{bond} (kcal/mol)
1−1	[1$\bar{1}$1]	−11.56
1−1	[001]	−7.89
1−1	[1$\bar{0}$0]	−6.13
1−1	[$\bar{1}$10]	−4.03
1−1	[101]	−3.82
1−1	[0$\bar{1}$0]	−3.53
1−1	[0$\bar{1}$1]	−1.41

[a] The lattice translation denotes the unit cell in which the second growth unit (GU2) is positioned relative to the first growth unit (GU1), which is in [000] by definition. The full crystal graph is produced by applying the self-inversion symmetry to the bonds (i.e., 1−1 [001] implies that 1−1 [00$\bar{1}$] also exists).

TABLE 4: Reduced Crystal Graph of the $P2_1$ Structure[a]

GU1−GU2	translation	E_{bond} (kcal/mol)	GU1−GU2	translation	E_{bond} (kcal/mol)
1−2	[10$\bar{1}$]	−8.52	1−4	[1$\bar{1}$1]	−3.69
1−4	[0$\bar{1}$0]	−8.41	1−2	[000]	−3.27
2−2	[001]	−7.65	1−1	[101]	−2.49
1−1	[001]	−6.29	1−2	[100]	−2.43
2−2	[100]	−6.28	1−2	[00$\bar{1}$]	−2.22
1−1	[1$\bar{0}$0]	−6.00	1−4	[1$\bar{1}$0]	−2.03
1−4	[0$\bar{1}$1]	−3.83	2−2	[$\bar{1}$01]	−0.68
2−2	[101]	−3.78	1−1	[$\bar{1}$01]	−0.63

[a] The full crystal graph is produced by applying the screw axis on the growth units as well as the bond inversion. Growth units are numbered according to the numbering of the layers in Figure 1.

TABLE 5: Connected Nets of the Forms {*hkl*}, Interplanar Distance, Number of Connected Nets in Form {*hkl*}, and Energy of the Connected Net with the Lowest Attachment Energy of the *P*1 Phase

{*hkl*}	*d* (Å)	no.	E_{att} (kcal/mol)
{110}	6.019	1	−14.89
{01$\bar{1}$}	5.475	1	−19.27
{10$\bar{1}$}	5.045	1	−19.45
{010}	10.191	1	−20.53
{001}	6.627	1	−24.68
{100}	6.417	1	−25.53
{11$\bar{1}$}	4.900	1	−30.52
{1$\bar{1}$1}	4.114	1	−32.93
{1$\bar{1}$$\bar{1}$}	4.218	1	−33.13

or etch phenomenon. Visual inspection and comparison of many crystals in various stages of development led to the conclusion that the pits must initiate throughout the experiments. Some pits were found to extend almost entirely through the crystals, whereas some were very shallow. Therefore, we conclude that the growth pits must be a growth phenomenon. Thus, the formed pits are an indication that surface-specific growth hampering caused the pit patterns on the (010) face.

4.2. Computational Results. The results of the Hartman−Perdok analysis are summarized in Tables 3−6 and Figure 5. Initially, Bravais−Friedel−Donnay−Harker (BFDH) morphologies of both polymorphs were calculated[17−19] to get a first impression. However, neither resembled any of the grown crystals. In contrast, the morphologies calculated using the HP/E_{att} method can be easily correlated to the respective morphologies. The platelike morphology, which was calculated for the $P2_1$ polymorph, is in reasonable agreement with the crystals grown from acetone. The method correctly predicts the presence of the {020}, {001}, {100}, and {10$\bar{1}$} forms, but the aspect ratio of the predicted morphology is much smaller. This is typical for the use of the attachment energy as a parameter for the growth rate of a form. The larger aspect ratio of the

TABLE 6: Connected Nets of the Forms {*hkl*}, Interplanar Distance, Number of Connected Nets in Form {*hkl*}, and Energy of the Connected Net with the Lowest Attachment Energy of the $P2_1$ Phase

{*hkl*}	*d* (Å)	no.	E_{att} (kcal/mol)	{*hkl*}	*d* (Å)	no.	E_{att} (kcal/mol)
{020}[a]	20.733	4	−32.86	{11$\bar{1}$}	5.156	16	−84.35
{040}	10.367	4	−62.80	{12$\bar{1}$}	5.040	10	−93.70
{100}	6.580	6	−62.14	{101}	4.256	19	−99.90
{110}	6.498	4	−67.60	{11$\bar{1}$}	4.234	16	−102.44
{001}	6.590	6	−69.47	{13$\bar{1}$}	4.864	4	−103.26
{011}	6.509	4	−72.39	{121}	4.169	10	−104.62
{12$\bar{0}$}	6.271	1	−74.12	{131}	4.067	4	−107.69
{10$\bar{1}$}	5.196	19	−76.08	{14$\bar{1}$}	3.937	1	−109.87
{021}	6.281	1	−77.44	{14$\bar{1}$}	4.645	1	−113.33

[a] The attachment energy of the (020) face is arguable (see text).

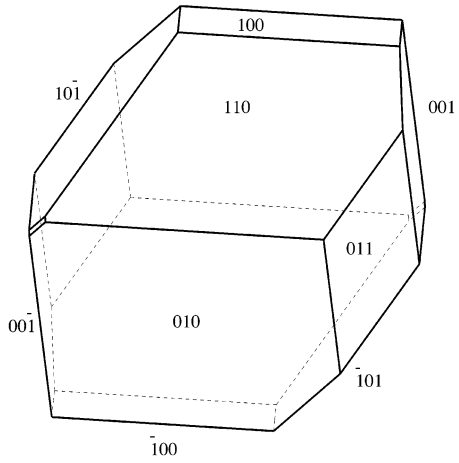

(a) *P*1

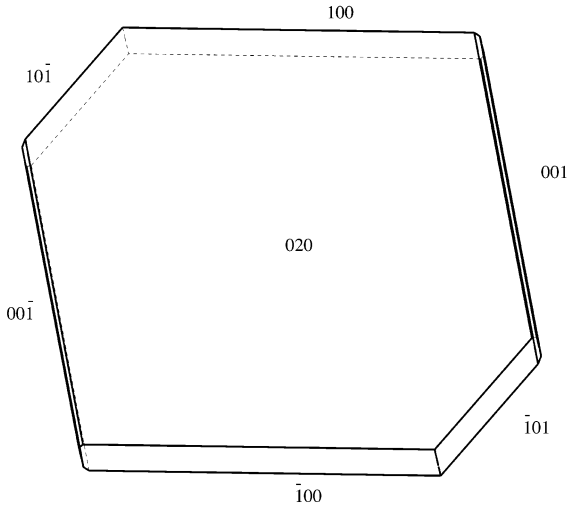

(b) $P2_1$

Figure 5. Calculated Hartman−Perdok morphologies of the polymorphs of 7αMNa based on the HP/E_{att} assumption.

experimentally observed crystals is caused by the larger growth rates of the {100} faces relative to {001}. The blocklike appearance of the calculated *P*1 morphology remarkably resembles the vapor-grown crystals. Raman spectroscopy revealed that the polymorph grown was $P2_1$, however. The *P*1 morphology in Figure 5a is rotated to match the orientation of the crystal in Figure 4. Visually, these almost perfectly match except for the absence of the face (001), which is probably accidental because the (00$\bar{1}$) is present (see Figure 4).

Comparing parts a and b of Figure 5 shows that most forms of the calculated *P*1 morphology correspond to those of the

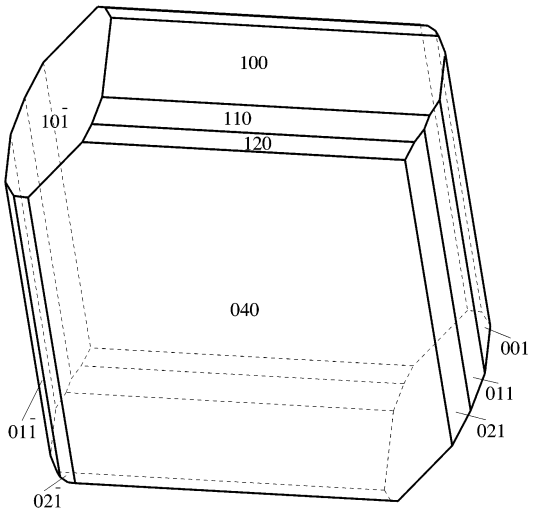

Figure 6. Artificial morphology after deleting the {020} form from the $P2_1$ morphology of Figure 5b. It is clear that this morphology does not show better resemblance to the experimental morphology in Figure 4.

calculated $P2_1$ morphology, except for the {011} and {110}, which do not appear on that morphology. This seems to be caused by the fact that the morphological importance of the $P2_1${020} form is much bigger than that of the $P1${010} form, which is due to Friedels law or more generally to the BFDH selection rules[18−20] ({020} instead of {010}) and the geometry of the unit cell. Comparing the crystal graphs of the $P1$ and $P2_1$ structures, the latter can be regarded as having a translational pseudosymmetry along the *b* axis in terms of bond energies. This also follows directly from the partly isostructural layers as described in section 2. A correction for this difference can be applied by disallowing {020} and taking the form {040} into consideration, which effectively doubles the thickness of the morphology. This results in the artificial morphology of Figure 6, which has too many faces due to the higher symmetry. Clearly, the morphological anomaly of the vapor-grown crystals resembling the calculated triclinic morphology cannot be explained by this energetic pseudosymmetry effect. Considerable effort was put into finding a better morphological description of the observed crystals according to the $P2_1$ structure. However, this led to very improbable morphologies because practically all crystal faces had to be severely tampered with. Moreover, many nonconnected faces with high indices and high attachment energies would dominate the crystals, resulting in a large total surface energy. On the other hand, the morphological description based on the attachment energies of the $P1$ structure is straightforward, contains all of the low attachment energy connected net orientations, and does not need any adjustments of the morphological importances after applying the attachment energy criteria for the relative growth rates.

5. Discussion and Conclusions

The platelike 7αMNa crystals grown from acetone solution were found to grow as $P2_1$ where the morphology corresponds well to the calculated morphology except for a slight difference in aspect ratio. Therefore, vapor-growth experiments were conducted to see whether that difference is caused by the solvent. However, the morphology obtained from the vapor phase showed to be completely different. The difference might be argued to be caused by the difference in supersaturation. However, in our previous work, we observed crystals grown from a very large range of supersaturations. None of those crystals resembled the morphology of the vapor-grown crystals. This effectively rules out the supersaturation as the cause of the morphological discrepancy.

It is shown that the morphology of crystals grown from the vapor phase best fits the $P2_1$ lattice and indeed the crystals were confirmed to consist of this polymorph by Raman spectroscopy. However, this morphology shows little resemblance to the morphology obtained from solution nor to the calculated morphology of this polymorph. Although the orientation of the crystal faces fit much worse to the $P1$ setting, the overall appearance of the crystals is strikingly identical to the calculated $P1$ morphology. This anomalous behavior can be regarded as pseudomorphism. As McCrone described it,[21]

"A pseudomorph is a transformed crystal: the external shape of the original crystal may be discernible even though the internal structure is that of the new form. The pseudomorph may be more or less broken up by the transition if the density difference between the two forms is very great."

Clearly, the established morphology prediction methods cannot predict the correct morphology for these particular crystals. The usage of the attachment energy as a measure for the rate of growth without consideration of the growth mechanism and crystal structure is already subject to discussion[16,22−27] because none of those methods take supersaturation and kinetics into account. Considering the {040} instead of the {020} form did not improve the resemblance much. In fact, trying to mimic the experimental morphology using the $P2_1$ crystal structure led to highly unlikely face indices and could still not produce the shapes of the various forms {*hkl*} very well. Clearly, we found a pseudomorphic system, causing the strong resemblance to the calculated $P1$ morphology. This implies that the $P1$ phase must play an important role in the crystal growth prior to the formation of the $P2_1$ phase. Ruling out the effect of supersaturation, we can only explain this by surface kinetics.

As was shown in our previous work, in acetone, the growth kinetics of the $P1$ phase are favored at higher supersaturation.[6] The present experimental setup does not allow us to calculate the absolute supersaturation at a specific spot on the copper substrate, disallowing quantitative comparison to the acetone supersaturation. Also, it is doubtful whether such an absolute comparison would make sense in the first place because the mobility kinetics are probably the main cause of the observed differences. This means that our results have to be interpreted from a qualitative point of view. The most important observation in our previous work concerns the combination of 2D and 3D nucleation and mobility kinetics; the latter are distinguished as the combined effect of transport of the growth units and their conformational freedom. It was shown that the metastable zone for heterogeneous 2D nucleation of the metastable polymorph (i.e., $P1$) on the (010) face of the $P2_1$ phase was only slightly higher than that of the homogeneous 2D nucleation of the stable polymorph (i.e., $P2_1$). The mobility kinetics of the growth after the 2D nucleation turned out to be more favorable for the $P1$ phase using that nucleation mechanism. Without the mediating role of the solvent, mobility kinetics are expected to play an even more dominant role in the growth of the vapor-grown crystals. This is caused by the fact that the $P1$ conformation of the molecules in the vapor phase is the most stable, as was calculated by conformational analysis and molecular dynamics of the molecules in the vapor phase. This suggests that the $P1$ polymorph is favored in terms of growth kinetics in the vapor phase even more, causing heterogeneous, polymorphic 2D nucleation to take place. After nucleation, growth of the metastable $P1$ phase takes place more rapidly than that of the

$P2_1$ phase. Hence, we conclude that the crystal surface must indeed be dominated by growth of the *P*1 phase, which explains our morphologic observations. Raman spectroscopy showed these crystals to be in the $P2_1$ phase after the growth experiments. This means that the *P*1 surface layer transformed into $P2_1$. It is unclear exactly at which stage the transformation took place because the vapor growth could not be monitored in situ. However, differential scanning calorimetry (DSC) experiments learned that without a mediating solvent *P*1 only transforms into $P2_1$ at high temperature (417 K; 26 K below the melting point of $P2_1$).[6] The furnace temperature was at least 34 K below the spontaneous transformation temperature. At room temperature, *P*1 crystals were shown to be stable for years. Only in the presence of acetone, the transformation could be observed on a time scale of 24−48 h.[6] Hence, the transformation must already take place during the growth experiments at the higher temperatures.

Although pseudomorphism is a plausible explanation for the observed morphology, it does not explain the distinctive occurrence of the faceted pits on the crystals. It is very important to note that these pits only appear on one specific face. According to the morphology calculations, morphology measurements, and determination of the absolute configuration of the crystal structure versus the morphology by single-crystal X-ray diffraction, this face corresponds to the carbonyl-terminated (020) face on the $P2_1$ morphology and to the (010) face of *P*1, after the crystallographic transformation. It is exactly this face that shows the epitaxial polymorphic growth in acetone at high supersaturations. It was shown that this is caused by the small structural differences between the phases, which may cause susceptibility to polymorphic behavior in the first place. The appearance of the pits indicates that either of two effects may take place, or perhaps even a combination thereof. First of all, the creation of the $P2_1$ phase from the *P*1 phase requires rotation of the molecules around the *b* axis. This introduces the possibility of growth domains. At the domain borders, a defect layer will cause stacking faults. This relates to McCrone's statement about the instability of pseudomorphs. Indeed our crystals occasionally cracked up. Although in our case the density difference is small (1.2%), it is possible that the growth pits are a result from stress within the crystals hampering further growth. However, one might expect to see the result of this effect on more than one specific crystal facet and certainly on the opposite crystal face $(0\bar{1}0)$. The implication of the isostructural substructure shows in the repetition of orientations of the molecules along the (010) layers. The formation of the $P2_1$ structure requires the perfect repetition of molecular orientation according to the pattern ···FBBFFBBF···, whereas the *P*1 structure has only one relative orientation of the molecules. It can thus easily be understood that domains can be formed as a result of the dominating mobility kinetics, which does not allow for the full relaxation into the perfect repetition, for instance, ···FBFFBBF···, where the relative orientation of the molecules changes too quickly. This is recognized as polytypism and was calculated to result in a minor enthalpic deficiency on the order of 1 kJ/mol per molecular unit area of the layer−layer interaction. This certainly coincides with the low barrier for heterogeneous 2D nucleation causing the polymorphic epitaxial growth described earlier and could also likely contribute to the formation of growth defects causing the observed faceted pits.

Alternatively, impurities may block the growth at the surface causing the growth pits to occur. These impurities would be caused by the deterioration of the steroid due to the temperature of the furnace. At high temperature, 7αMNa is known to be susceptible to a rearrangement on the A-ring of the double bond from carbon atoms 5-10 to 4-5[6] producing the native compound 7-α-methyl norethindrone (7αMN). This bond rearrangement causes ring A to lose its flexibility, which is needed in the $P2_1$ structure. The unpublished crystal structure of 7αMN is also $P2_1$, but no interstitial stabilizing layers are found as in the 7αMNa structure. It can be concluded that the rearrangement influences the flexibility and directionality of the hydrogen-bond-forming carbonyl, hampering the continuation of the $P2_1$ crystal structure. This would typically promote the formation of stacking faults of the type ···FBBBFFB···, where the relative orientation of the molecules is favored not to change between the layers. Because (010) is the carbonyl-terminated face, this could indeed explain why only this face shows the growth pits. Therefore, we believe the impurity effect is the more likely explanation of the pit patterns, although further research would be needed to confirm the true cause of the polytypic stacking faults.

To summarize, the following can be concluded concerning the growth mechanism of crystals of our model compound grown from the vapor phase. Although vapor growth was expected to produce a close resemblance to the calculated morphology, the rare phenomenon of pseudomorphism took place. This anomalous behavior results in crystals of the $P2_1$ phase, which possess the appearance of the *P*1 phase. This can be explained by the fact that the growth kinetics of the $P2_1$ phase are favored by nucleation of the *P*1 phase combined with transformation into $P2_1$. It was shown in detail that polytypic stacking faults are causing growth hampering causing an irregular pit pattern at the (010) face of the vapor-grown crystals.

Acknowledgment. The authors thank Gertjan Bögels for cooperating with the vapor growth experiments, Willem van Enckevort for fruitful discussions, and Organon, N.V., for experimental and scientific backup and providing the title compound. This research was supported financially by Organon, N.V., through the Council for Chemical Sciences of The Netherlands Organization for Scientific Research (CW-NWO) in the framework of the PPM/CMS crystallization project.

References and Notes

(1) Bernstein, J.; Davey, R. J.; Henck, J.-O. *Angew. Chem., Int. Ed.* **1999**, *38*, 3440−3461.

(2) Allen, F. H.; Kennard, O. *Chem. Des. Autom. News* **1993**, *8* (1), 1, 31−37.

(3) Allen, F. H.; Kennard, O.; Taylor, R. *Acc. Chem. Res.* **1983**, *16*, 146−153.

(4) Declercq, J.-P.; van Meerssche, M. *Recl. Trav. Chim. Pays-Bas* **1984**, *103*, 145−147.

(5) Declercq, J.-P.; van Meerssche, M.; Zeelen, F. J. *J. R. Neth. Chem. Soc.* **1984**, *103* (5), 145.

(6) Boerrigter, S. X. M.; van den Hoogenhof, C. J. M.; Meekes, H.; Bennema, P.; Vlieg, E.; van Hoof, P. J. C. M. *J. Phys. Chem. B* **2002**, *106* (18), 4725−4731.

(7) Bögels, G.; Meekes, H.; Bennema, P.; Bollen, D. *Philos. Mag. A* **1999**, *79*, 639−653.

(8) Mayo, S. L.; Olafson, B. D.; Goddard, W. A. *J. Phys. Chem.* **1990**, *94*, 8897−8909.

(9) Bayly, C. I.; Cieplak, P.; Cornell, W. D.; Kollman, P. A. *J. Phys. Chem.* **1993**, *97* (40), 10269−10280.

(10) Frisch, M. J.; Trucks, G. W.; Schlegel, H. B.; Gill, P. M. W.; Johnson, B. G.; Robb, M. A.; Cheeseman, J. R.; Keith, T.; Petersson, G. A.; Montgomery, J. A.; Raghavachari, K.; Al-Laham, M. A.; Zakrzewski, V. G.; Ortiz, J. V.; Foresman, J. B.; Cioslowski, J.; Stefanov, B. B.; Nanayakkara, A.; Challacombe, M.; Peng, C. Y.; Ayala, P. Y.; Chen, W.; Wong, M. W.; Andres, J. L.; Replogle, E. S.; Gomperts, R.; Martin, R. L.; Fox, D. J.; Binkley, J. S.; Defrees, J. D.; Baker, J.; Stewart, J. P.; Head-Gordon, M.; Gonzalez, C.; Pople, J. A. *Gaussian 94*, revision D.4; Gaussian, Inc.: Pittsburgh, PA, 1995.

(11) Grimbergen, R. F. P.; Reedijk, M. F.; Meekes, H.; Bennema, P. *J. Phys. Chem. B* **1998**, *102*, 2646−2653.
(12) Boerrigter S. X. M., Grimbergen R. F. P.; Meekes H. *FACELIFT-2.50, a Program for Connected Net Analysis*; Department of Solid State Chemistry, University of Nijmegen: Nijmegen, The Netherlands, Feb. 2001; mail to hugom@sci.kun.nl.
(13) Hartman, P.; Perdok, W. G. *Acta Crystallogr.* **1955**, *8*, 49−52.
(14) Hartman, P.; Perdok, W. G. *Acta Crystallogr.* **1955**, *8*, 521−524.
(15) Hartman, P.; Perdok, W. G. *Acta Crystallogr.* **1955**, *8*, 525−529.
(16) Grimbergen, R. F. P.; Meekes, H.; Bennema, P.; Strom, C. S.; Vogels, L. J. P. *Acta Crystallogr. A* **1998**, *54*, 491−500.
(17) *Cerius*^{2} *User Guide*, version 3.8; Molecular Simulations Inc.: San Diego, CA, 1998.
(18) Donnay, J. D. H.; Harker, D. *Am. Mineral.* **1937**, *22*, 446−467.
(19) Donnay, J. D. H.; Donnay, G. *C. R. Acad. Sci. Paris* **1961**, *252*, 908−909.
(20) Friedel, G. *Leçon de Cristallographie*; Hermann: Paris, 1911.
(21) McCrone, W. C. In *Physics and Chemistry of the Organic Solid State*; Fox, D., Labes, M. M., Weissberger, A., Eds.; John Wiley & Sons: New York, 1965; Vol. 2, Chapter 8, pp 725−767.
(22) Meekes, H.; Bennema, P.; Grimbergen, R. F. P. *Acta Crystallogr. A* **1998**, *54*, 501−510.
(23) Grimbergen, R. F. P.; Bennema, P.; Meekes, H. *Acta Crystallogr. A* **1999**, *55*, 84−94.
(24) Hollander, F. F. A.; Boerrigter, S. X. M.; van de Streek, J.; Grimbergen, R. F. P.; Meekes, H.; Bennema, P. *J. Phys. Chem. B* **1999**, *103*, 8301−8309.
(25) Sweegers, C.; Boerrigter, S. X. M.; Grimbergen, R. F. P.; Meekes, H.; Flemming, S.; Hiralal, I. D. K.; Rijkeboer, A. *J. Phys. Chem. B* **2002**, *106* (5), 1004−1012.
(26) Boerrigter, S. X. M.; Hollander, F. F. A.; van de Streek, J.; Bennema, P.; Meekes, H. *Cryst. Growth Des.* **2002**, *2* (1), 51−54.
(27) Boerrigter, S. X. M.; Cuppen, H. M.; Ristic, R. I.; Sherwood, J. N.; Bennema, P.; Meekes, H. *Cryst. Growth Des.* **2002**, *2* (5), 357−361.